

Quantifying axonal features of human superficial white matter from three-dimensional multibeam serial electron microscopy data assisted by deep learning

Qiyuan Tian^{a,b,c,*} , Chanon Ngamsombat^{b,d} , Hong-Hsi Lee^{b,c} , Daniel R. Berger^e , Yuelong Wu^e , Qiuyun Fan^{b,c}, Berkin Bilgic^{b,c}, Ziyu Li^f, Dmitry S. Novikov^{g,h}, Els Fieremans^{g,h} , Bruce R. Rosen^{b,c}, Jeff W. Lichtman^e , Susie Y. Huang^{b,c}

^a School of Biomedical Engineering, Tsinghua University, Beijing, PR China

^b Athinoula A. Martinos Center for Biomedical Imaging, Department of Radiology, Massachusetts General Hospital, Charlestown, MA, USA

^c Harvard Medical School, Boston, MA, USA

^d Department of Radiology, Faculty of Medicine, Siriraj Hospital, Mahidol University, Thailand

^e Department of Molecular and Cellular Biology, Harvard University, Cambridge, MA, USA

^f Nuffield Department of Clinical Neurosciences, University of Oxford, Oxford, UK

^g Department of Radiology, Center for Biomedical Imaging, New York University School of Medicine, NY, NY, USA

^h Center for Advanced Imaging Innovation and Research (CAI2R), New York University School of Medicine, NY, NY, USA

ARTICLE INFO

Keywords:

Short-range association fiber

Axon diameter

G-ratio

Along-axon variation

Convolutional neural network

Transfer learning

ABSTRACT

Short-range association fibers located in the superficial white matter play an important role in mediating higher-order cognitive function in humans. Detailed morphological characterization of short-range association fibers at the microscopic level promises to yield important insights into the axonal features driving cortico-cortical connectivity in the human brain yet has been difficult to achieve to date due to the challenges of imaging at nanometer-scale resolution over large tissue volumes. This work presents results from multi-beam scanning electron microscopy (EM) data acquired at $4 \times 4 \times 33 \text{ nm}^3$ resolution in a volume of human superficial white matter measuring $200 \times 200 \times 112 \mu\text{m}^3$, leveraging automated analysis methods. Myelin and myelinated axons were automatically segmented using deep convolutional neural networks (CNNs), assisted by transfer learning and dropout regularization techniques. A total of 128,285 myelinated axons were segmented, of which 70,321 and 2102 were longer than 10 and 100 μm , respectively. Marked local variations in diameter (i.e., beading) and direction (i.e., undulation) were observed along the length of individual axons. Myelinated axons longer than 10 μm had inner diameters around 0.5 μm , outer diameters around 1 μm , and g-ratios around 0.5. This work fills a gap in knowledge of axonal morphometry in the superficial white matter and provides a large 3D human EM dataset and accurate segmentation results for a variety of future studies in different fields.

1. Introduction

Short-range association fibers (SAFs) ranging in length from 3 to 30 mm connect neighboring cortical areas within a single lobe or across lobes and play an important role in mediating cortico-cortical connectivity in humans. SAFs reside in the thin layer ($\sim 1.5 \text{ mm}$) of superficial white matter immediately beneath the infragranular layer of the cortex. These fibers, also known as U-fibers, follow the highly convoluted cortical manifold and are estimated to occupy 240 out of 420 cm^3 of the entire human cortical white matter volume (Schüz and Braitenberg,

2002; Markov et al., 2013; Braitenberg and Schüz, 2013). SAFs contribute to approximately 90 % of all white matter connections (Schüz and Braitenberg, 2002) and have a central role in mediating higher-order cognitive function in humans. They are among the slowest to myelinate and remain incompletely myelinated until the fourth decade of life (Barkovich, 2000; Parazzini et al., 2002; Wu et al., 2016). SAFs are also less myelinated compared to long-range fiber tracts in the deep white matter, which renders SAFs more vulnerable to damage (Butt and Berry, 2000) in neurological and psychiatric diseases such as multiple sclerosis (Van der Knaap and Valk, 2005), progressive multifocal

* Corresponding author at: Center for Biomedical Imaging Research at Tsinghua University, 30 Shuangqing Road, Haidian District, Beijing, PR China, 100084.

E-mail address: qiuyantian@tsinghua.edu.cn (Q. Tian).

<https://doi.org/10.1016/j.neuroimage.2025.121212>

Received 4 July 2024; Received in revised form 8 April 2025; Accepted 11 April 2025

Available online 11 April 2025

1053-8119/© 2025 The Authors. Published by Elsevier Inc. This is an open access article under the CC BY-NC-ND license (<http://creativecommons.org/licenses/by-nc-nd/4.0/>).

leukoencephalopathy (Van der Knaap and Valk, 2005), Alzheimer's disease (Phillips et al., 2016), schizophrenia (Phillips et al., 2011; Nazeri et al., 2013), and autism spectrum disorder (Sundaram et al., 2008; Shukla et al., 2011). Elucidating the properties of SAFs such as axon diameter and g-ratio (defined as the ratio of the inner to outer diameter of the myelin sheath), which determine the axonal conduction velocity, promises to advance a greater understanding of the role of SAFs in cognitive function and their alteration in development, aging and various brain disorders.

Electron microscopy (EM) acquires images of brain tissue samples at nanometer resolution and offers a useful tool for investigating the properties of SAFs. Previous EM studies (Aboitiz et al., 1992a; Liewald et al., 2014a) of human corpus callosum, superior longitudinal fascicle, uncinate and inferior occipitofrontal fascicle have revealed distinctive axon diameters in different parts of the corpus callosum and shown that most myelinated axons have inner diameters below 1 μm . EM measurements of axon diameter have also been acquired in post-mortem porcine optic and sciatic nerves and spinal cord (Assaf et al., 2008) as well as murine corpus callosum (Barazany et al., 2009; Veraart et al., 2020; Sepehrband et al., 2016) samples as the gold standard for validating indirect measurements of relative axonal size and density from diffusion magnetic resonance imaging (MRI). Nonetheless, the EM in these works was only performed in 2D. Perge et al. acquired 3D EM data in guinea pigs to investigate how optic nerves use space and energy, finding that optic axons are mostly thin with a skewed distribution peaking at 0.7 μm (Perge et al., 2009). More recently, axons have been reconstructed from 3D EM data of murine brain samples to provide realistic white matter substrates for Monte Carlo simulations of water diffusion for developing and validating new diffusion MRI biophysical modeling methods (Lee et al., 2019; Lee et al., 2020a,b; Nguyen et al., 2018; Andersson et al., 2022). The development of high-throughput multibeam serial EM (Eberle and Zeidler, 2018) has rendered the acquisition of high-resolution images at nanometer resolution over much larger tissue volumes, i.e., hundreds of microns, more feasible.

Nevertheless, the segmentation of axons in large 3D EM datasets poses a major challenge. Due to the large data size, manual segmentation is challenging, if not impossible, as it is extremely labor intensive and time consuming. Many automated or semi-automated EM segmentation tools based on conventional algorithms have been released for segmenting gray matter (Dorkenwald et al., 2017; Kaynig et al., 2015; Sommer et al., 2011; Januszewski et al., 2018; Berger et al., 2018) and white matter (Lee et al., 2019; Sommer et al., 2011; Kleinnijhuis, 2017; Abdollahzadeh et al., 2019; Jurrus et al., 2009) images. Recent advances in high-performance computing hardware and deep learning offer a more powerful computational tool for image segmentation and have been widely adopted for segmenting biomedical imaging data (Ronneberger et al., 2015; Falk et al., 2019) including EM images of murine brain tissue samples (Berning et al., 2015; Abdollahzadeh et al., 2021; Zaimi et al., 2018; Motta et al., 2019).

Recently, a millimeter cubic volume of human cerebral cortex extending through all cortical layers and including the adjacent superficial white matter was imaged using high-throughput multibeam serial EM technology (Shapson-Coe et al., 2024), providing a unique opportunity for investigating the properties of SAFs at nanometer spatial resolution. We sought to segment all myelinated axons in a large sub-volume measuring up to $200 \times 200 \times 112 \mu\text{m}^3$ of superficial white matter for characterizing the morphology of the human SAFs at a high-resolution of $32 \times 32 \times 33 \text{ nm}^3$. To achieve this goal, we used state-of-the-art deep learning techniques, deploying convolutional neural networks (CNNs) for the segmentation and incorporating transfer learning and Monte Carlo dropout to deal with the lack of extensive reference segmentation for training. The EM data and the segmentation results are publicly available, for various potential applications such as providing a large dataset for training sophisticated CNNs in other human EM studies, serving as a test bed for developing new segmentation and axonal morphometry quantification algorithms, and enabling realistic

human brain 3D water diffusion simulation for deepening our understanding of effects of axonal features on diffusion MRI modeling methods (Lee et al., 2024) and accelerating their clinical application and translation.

2. Methods

2.1. Data description

This study used a published, de-identified, and publicly available EM dataset for image analysis (Shapson-Coe et al., 2024) (<https://h01-release.storage.googleapis.com/data.html>). The brain tissue sample preparation and data acquisition were described in detail previously (Shapson-Coe et al., 2024) and are briefly summarized as below. A sample of human brain tissue was obtained intraoperatively from the left anterior portion of the middle temporal lobe of a 45-year-old female with drug-resistant epilepsy who underwent surgery for removal of an epileptogenic focus in the left hippocampus. The excised tissue sample was remote from the epileptogenic focus and showed no diagnostic abnormality recognized by traditional neuropathology. Immediately following excision, the tissue sample was placed in glutaraldehyde/paraformaldehyde fixative, stained with reduced osmium tetroxide and embedded in Epon resin (Tapia et al., 2012). The cured block containing full-thickness cerebral cortex and a portion of superficial white matter was trimmed to a $2 \times 3 \text{ mm}^2$ rectangle and a depth of $\sim 200 \mu\text{m}$, sectioned with a custom-built automated tape-collecting ultramicrotome (ATUM) attached to a Leica UC6 ultramicrotome, and imaged using a high-speed multibeam scanning electron microscope (ZEISS MultiSEM) (Baena et al., 2019). A total of 5292 thin sections with an average section thickness of 33 nm (range 30–40 nm) were imaged at $4 \times 4 \text{ nm}^2$ resolution with an approximated data size of 350 gigabytes (GB) per section and 2.1 petabytes for all sections. The acquisition time was 326 days.

A subset of images centered in the superficial white matter (a volume of $200 \times 200 \times 175 \mu\text{m}^3$) was extracted from the entire dataset. To reduce the data size and computational load and to transform the data to approximately isotropic resolution, images were down-sampled to $32 \times 32 \text{ nm}^2$ in-plane resolution with a total data size approximating 177 GB. Several sections were missing and/or had limited image quality and were excluded from further processing and segmentation (sections 1700 to 1895). A total of 3397 consecutive sections (sections 1896 to 5292) were used. The dataset that was processed and segmented corresponded to a volume of $200 \times 200 \times 112 \mu\text{m}^3$ and was 113 GB in data size, with a matrix size of $6250 \times 6250 \times 3397$ and a resolution of $32 \times 32 \times 33 \text{ nm}^3$ (Fig. 1b and c). The image intensities were stored as 8-bit unsigned integers (ranging 0 through 255) in the Joint Photographic Experts Group (JPEG) format. Representative images are shown in Fig. 1 (Fig. 1d–h) with different types of common image artifacts contained in the data, including saturated pixels (Fig. 1d), missing pixels (Fig. 1e), covered textures (Fig. 1f), image breaks (Fig. 1g), and image misalignment (Fig. 1h), which posed challenges for delineating the underlying axonal geometry.

2.2. Myelin and axon segmentation

Automated analysis methods leveraging deep learning and CNNs were employed for segmenting the tissue into three labels, including myelin, intra-axonal space (IAS), and extra-axonal space (EAS). The EAS segmentation includes all space outside myelinated axons, including not only the extra-axonal space, but also unmyelinated axons, other cell types as well as vessels. Several U-Nets (Falk et al., 2019) with slightly varying architectures (Supplementary Information Fig. 1) were employed for different tasks in this study. The procedure is detailed in the Supplementary Information and briefly described here.

First, a training dataset with reference manual segmentation of myelin and IAS was created using an iterative semi-automated

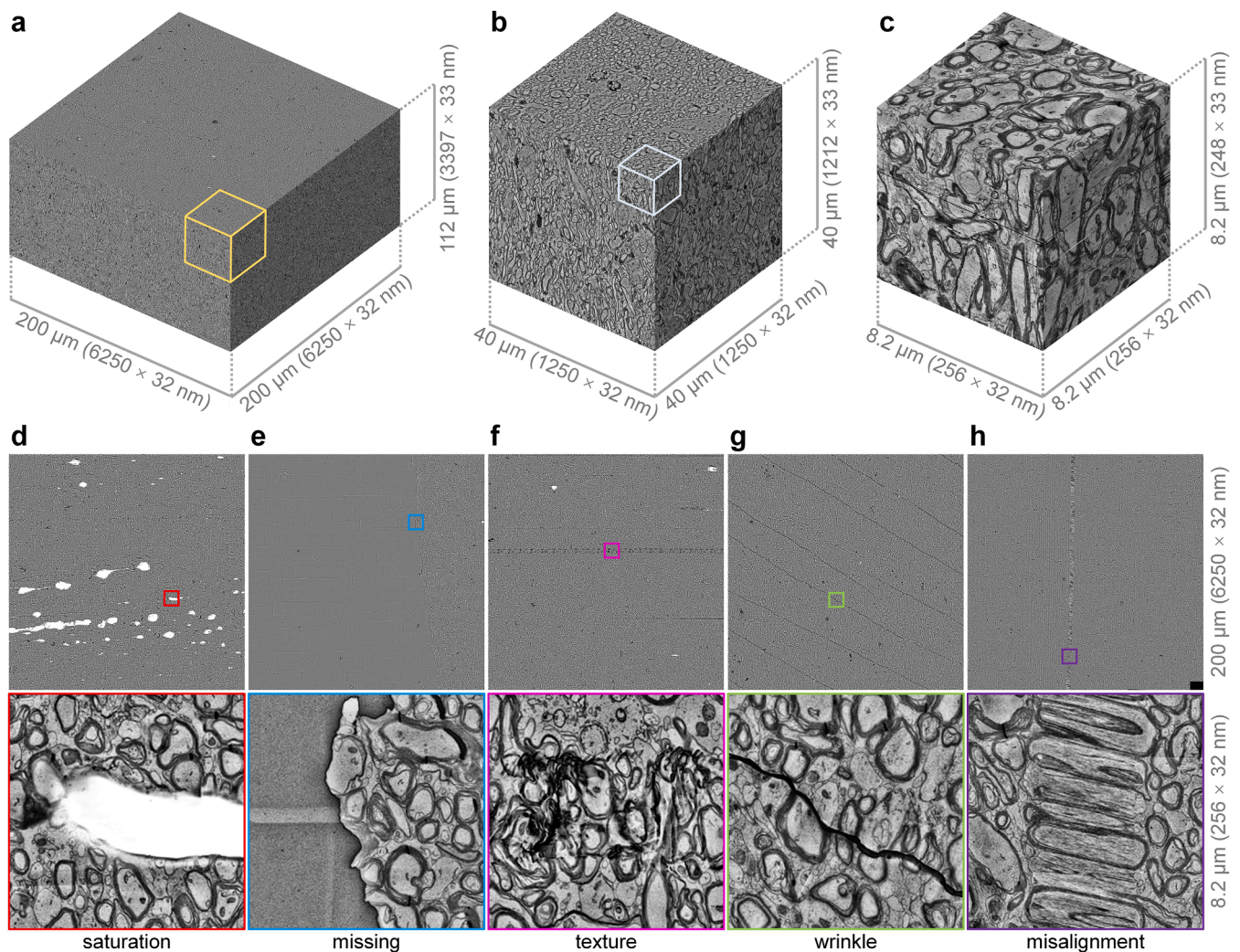


Fig. 1. Electron microscopy data. A large electron microscopy image volume of $200 \times 200 \times 112 \mu\text{m}^3$ size and $32 \times 32 \times 33 \text{ nm}^3$ resolution of superficial white matter in the human temporal lobe (a) and enlarged views of the top right corner (yellow box corresponding to b, light blue box corresponding to c). Representative images of $200 \times 200 \mu\text{m}^2$ size (6250×6250 matrix) with different types of image artifacts are displayed with enlarged views of image patches of $8.2 \times 8.2 \mu\text{m}^2$ size (256×256 matrix) (d–h).

segmentation strategy (Supplementary Information Fig. 2). At each iteration, an experienced neuroradiologist (C.N.) manually cleaned up initial segmentation results from an automated and well-performing method (i.e., a U-Net trained leveraging transfer learning), which substantially reduced the amount of manual work required by manual segmentation without any initialization. The created training dataset consisted of 1311 consecutive images ($43.3 \mu\text{m}$ thick) of $8.2 \times 8.2 \mu\text{m}^2$ size (256×256 matrix size) from a selected region with fewer image artifacts. The creation of the training dataset took a total of ~ 21 days for manual clean-up plus extra time for training and applying the U-Nets and data organization. The manual annotations were cross-checked by another neuroimaging researcher (Q.T.). The bottom 160 images out of 1311 images were preserved for evaluating the segmentation performance while the remaining 1151 images were used for training and validation.

Second, regions with image artifacts in the entire EM data were automatically identified using a 2D U-Net. For training this U-Net, reference masks of artifactual regions were generated using an automated image processing approach based on the image similarity between an image and its neighbors in a subset of the data, which were slightly cleaned up manually (Q.T.). The training dataset consisted of 2650 images (256×256 matrix size). Image artifacts were identified in 810 images, with 18.67 % artifactual pixels.

Finally, a 3D U-Net with dropout layers was trained, validated, and applied for generating probability values for the myelin, IAS, and EAS labels at each image pixel. For the training, input image volumes ($160 \times 160 \times 160$ matrix size) in the training dataset were flipped, rotated, and multiplied with the inverse of the image artifact masks randomly selected from the detected masks of all 3397 images to set a portion of the voxels to zero, for data augmentation, mimicking the dropout process, as well as providing the U-Net with information on the image artifacts contained in the data during the training. Each pixel was classified as the label with the highest probability predicted by the U-Net. The entire inference process took 40 days on two Tesla V100 graphics processing units (GPUs) (NVIDIA, Santa Clara, California).

2.3. Segmentation clean-up

The binarized masks corresponding to each tissue label generated by the U-Net results were further cleaned up based on the morphological properties of tissue type and the CNN-estimated probability. First, any area labeled as IAS with < 100 pixels was re-classified as myelin if the number of myelin pixels within a bounding box (the smallest box containing the region dilated by one pixel along each direction) was larger than the number of EAS pixels, and vice versa. The regions with any myelin-labeled tissue with < 100 pixels was re-classified in a similar

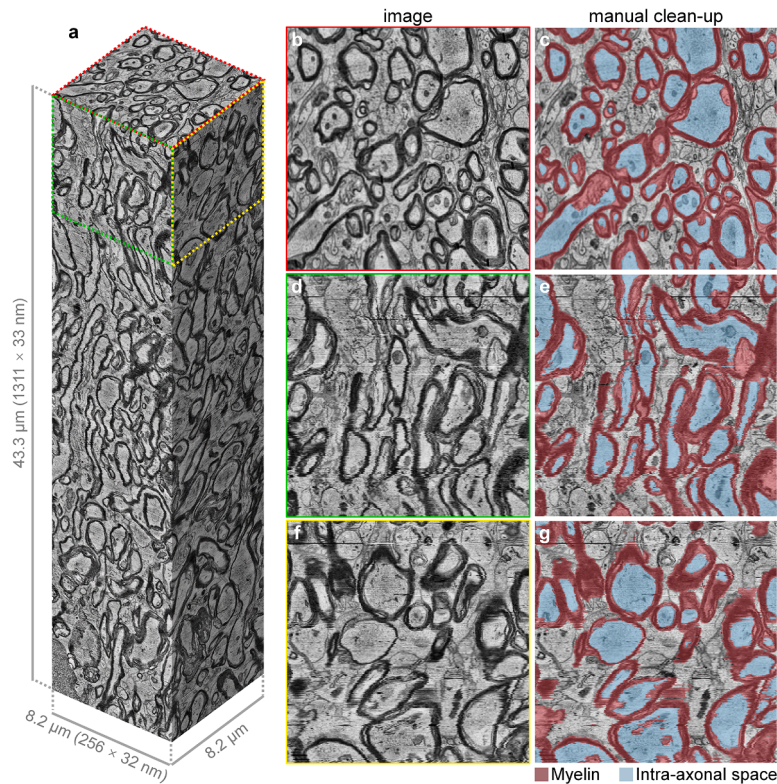


Fig. 2. Manual segmentation. The image volume of the training dataset (a) with manual segmentation of myelin and intra-axonal space from orthogonal views (b–g). This image volume was used to supervise the training of the 3D U-Net.

way. Second, any IAS-labeled tissue region shorter than $3.3 \mu\text{m}$ ($33 \text{ nm} \times 100$) was re-classified as myelin if the mean probability to be classified as myelin within this segment from the CNN was higher than the mean probability to be classified as EAS, and vice versa. The length of an IAS segment was estimated as the length of the major axis of the ellipsoid that had the same normalized second central moments as the IAS segment using the “regionprops3” function from the MATLAB software (MathWorks, Natick, Massachusetts) with the “PrincipalAxisLength” option.

2.4. Segmentation performance evaluation

The bottom 160 images (256×256 matrix size) out of 1311 images with manual segmentation from the training dataset were used for evaluating the performance of the U-Net segmentation. Segmentation results were generated by serial application of the trained U-Net and clean-up, as described in the previous sections. Dice coefficients between the U-Net and manual segmentation were computed for the segmented myelin, IAS and EAS.

2.5. Axonal feature quantification

Analysis tools in the Random Walker (RaW) segmentation software (Lee et al., 2019) (<https://github.com/NYU-DiffusionMRI/RaW-seg>) were used to quantify features of myelinated axons, including inner and outer axon diameters and g-ratios. Only the statistics from myelinated axons longer than $10 \mu\text{m}$ were used.

To quantify inner axon diameters, each IAS segment was rotated such that its major axis (i.e., computed using MATLAB’s “regionprops3” function with the “EigenVectors” option) was along the z-axis and the cross-sectional areas (Ω) of each slice perpendicular to the axonal skeleton (defined as the line connecting the center of mass of each slice) were calculated. The axon diameter was calculated as the diameter of a

circle with the same area Ω (i.e., $2\sqrt{\Omega/\pi}$). For each IAS segment, the mean and coefficient of variation (CV) (i.e., the ratio of the standard deviation to the mean) of axon diameters along the axonal skeleton were calculated to quantify the mean diameter and the along-axon diameter variation. For the quantification, the myelin, IAS and EAS segmentation results were down-sampled from $32 \times 32 \times 33 \text{ nm}^3$ resolution to $40 \times 40 \times 40 \text{ nm}^3$ resolution using nearest neighbor interpolation to reduce the data size to fit within the available CPU memory.

To quantify g-ratios (i.e., the ratio of the inner to outer axon diameter), adjacent myelinated axons with contact of their myelin sheaths were first automatically segmented using a non-weighted distance transform (i.e., MATLAB’s “bwdist” function) and watershed algorithm (i.e., MATLAB’s “watershed” function) on the CNN-segmented IAS masks. For each IAS segment and its surrounding myelin sheath, the inner and outer axon diameters were computed in a similar way at each point of the axonal skeleton derived from the IAS segment. The mean and CV of outer axon diameters and g-ratios along the axonal skeleton were calculated. For the quantification, segmentation results were down-sampled from $32 \times 32 \times 33 \text{ nm}^3$ resolution to $52 \times 52 \times 52 \text{ nm}^3$ resolution using nearest neighbor interpolation to accommodate the limited CPU memory.

The relationship between the g-ratio (g) and the inner diameter (d_{inner}) was derived leveraging the previously proposed log-linear relationship (Berthold et al., 1983; Little and Heath, 1994; West et al., 2015) between the number of myelin lamellae (n_1) and d_{inner} , i.e., $n_1 = C_0 + C_1 \cdot d_{\text{inner}} + C_2 \cdot \ln(d_{\text{inner}})$. In this study, the range of axon diameter of superficial white matter is narrow as suggested by the results (Fig. 7), centering around $0.5 \mu\text{m}$. Therefore, only a linear relationship was assumed, i.e., $n_1 = C_0 + C_1 \cdot d_{\text{inner}}$. C_0 , C_1 , C_2 are parameters that characterize the log-linear function. Assuming the width of each myelin lamellae is equal to k , the outer axon diameter $d_{\text{outer}} = d_{\text{inner}} + n_1 \cdot k = d_{\text{inner}} + C_0 \cdot k + C_1 \cdot k \cdot d_{\text{inner}}$. Therefore, the g-ratio $g = d_{\text{inner}} / d_{\text{outer}} = d_{\text{inner}} / [d_{\text{inner}} + C_0 \cdot k + C_1 \cdot k \cdot d_{\text{inner}}]$. The parameters (i.e., $C_0 \cdot k$ and C_1

· k) were fitted twice, using 10,000 pairs of d_{inner} and d_{outer} values randomly sampled from myelinated axons longer than 10 μm and 100 μm , respectively, using MATLAB's "fitlm" function.

3. Results

The efficient iterative semi-manual segmentation approach generated a high-quality training dataset consisting of reference segmentations of myelin and IAS with human-level accuracy (Fig. 2). This dataset was sufficient to optimize parameters of a segmentation CNN using the dropout technique. The bottom 100 consecutive images of the entire training dataset consisting of 1311 images and the manual segmentation are displayed in Supplementary Video 1.

Different types of image artifacts were accurately and robustly identified by visual inspection (Fig. 3a–f). For example, the wrinkles in the images resulted in nonlinear distortions (i.e., shrinkage) around the wrinkles (Fig. 3e). Therefore, in addition to the wrinkle itself, a narrow band along the direction of wrinkle was also identified as an artifactual region. The red arrowhead (Fig. 3f) highlights a horizontal region of misalignment (i.e., distorted axonal shape) that leads to nonlinear distortions within the entire field-of-view of the image patch, rendering the entire region misaligned with the adjacent slices and making this entire image patch an artifactual region.

The percentage of artifactual pixels within each of the 3397 images

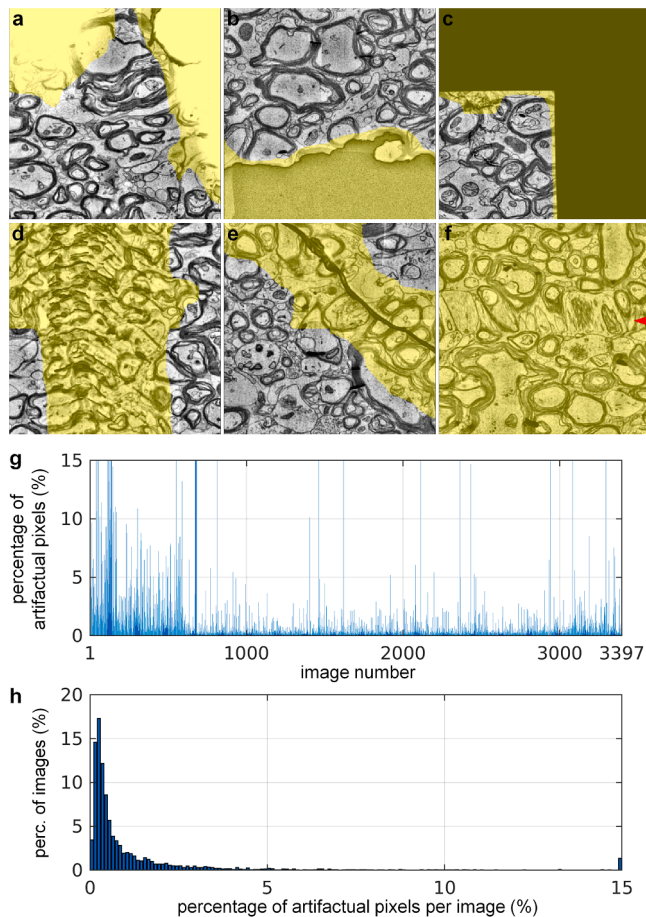


Fig. 3. Artifacts detection. Representative examples of different types of image artifacts detected by the U-Net are displayed (a–f, yellow region). For example, the red arrowhead (f) highlights a horizontal region of misalignment (i.e., distorted axonal shape) that leads to nonlinear distortions within the entire field-of-view of the image. The percentage of artifactual pixels in each of the 3397 images (g) and the histogram of the percentage of artifactual pixels per image are displayed (h).

(Fig. 3g) and the histogram of the percentage of artifactual pixels per image are shown (Fig. 3h). On average, 1.78 % of pixels were identified as artifactual pixels. Half of all images contained <0.5 % artifactual pixels and 90 % of all images contained <2.5 % artifactual pixels. The number of images with >15 %, 50 %, or 100 % of artifactual pixels was 46, 22 and 19, respectively.

The automated segmentation using CNN was highly similar to the manual segmentation, even in regions with images artifacts (Fig. 4). Quantitatively, the Dice coefficients between the CNN and manual segmentation results for the myelin, IAS and EAS were 0.9536, 0.9540, 0.9564 for the evaluation image volume. Fig. 5 displays an exemplary image volume of $20 \times 20 \times 20 \mu\text{m}^3$ size (Fig. 5a) and the IAS (Fig. 5b) and myelin (Fig. 5c) segmentation, the volume rendering of the IAS (Fig. 5d) and the IAS plus myelin segmentation (Fig. 5e), as well as the center of mass of each IAS segment (Fig. 5f). For the entire dataset, 42.29 %, 20.67 % and 37.04 % volumes were classified as myelin, IAS and EAS (all space outside myelinated axons, including extra-axonal space, unmyelinated axons, other cell types, and vessels) respectively.

A total of 128,285 IAS segments of myelinated axons were delineated, with 70,321 and 2102 axons longer than 10 and 100 μm , respectively. Forty randomly selected exemplary IAS segments longer than 100 μm with orientations approximately tangential to the cortical surface were volume rendered and shown in Fig. 6. These segments demonstrate local variations in diameter (i.e., beading) and direction (i.e., undulation) along the axon.

The histogram of the inner and outer axon diameters and the g-ratio, as well as the along-axon diameter variation of myelinated axons are shown in Fig. 7. For myelinated axons longer than 10 μm , the means (\pm standard deviation) were $0.53 \pm 0.17 \mu\text{m}$ and 0.53 ± 0.12 for the inner axon diameter and its CV, $0.99 \pm 0.20 \mu\text{m}$ and 0.31 ± 0.070 for the outer axon diameter and its CV, and 0.49 ± 0.058 for the g-ratio, respectively. The medians were 0.50 μm and 0.52 for the inner axon diameter and its CV, 0.95 μm and 0.31 for the outer axon diameter and its CV, and 0.49 for the g-ratio, respectively. The histograms of along-axon CV for inner (Fig. 7a, ii) and outer axon diameter (Fig. 7b, ii) show that myelinated axons are not perfect cylinders (i.e., along-axon diameter CV equal to 0).

For myelinated axons longer than 100 μm , the means (\pm standard deviation) were $0.76 \pm 0.28 \mu\text{m}$ and 0.45 ± 0.10 for the inner axon diameter and its CV, $1.27 \pm 0.32 \mu\text{m}$ and 0.29 ± 0.050 for the outer axon diameter and its CV, and 0.54 ± 0.052 for the g-ratio, respectively. The medians were 0.68 μm and 0.46 for the inner axon diameter and its CV, 1.19 μm and 0.29 for the outer axon diameter and its CV, and 0.54 for the g-ratio, respectively.

The relationship between the g-ratio and inner diameter (Fig. 7c, ii and c, iv) and between the inner diameter and myelin sheath thickness (Supplementary Information Fig. 4) for myelinated axons is displayed. The fitted parameters were $C_0 \cdot k = 0.21 \mu\text{m}$ and $C_1 \cdot k = 0.061$ for axons longer than 10 μm ($r = 0.31$, $p < 0.001$) and $C_0 \cdot k = 0.21 \mu\text{m}$ and $C_1 \cdot k = 0.095$ for axons longer than 100 μm ($r = 0.47$, $p < 0.001$), where k is the myelin lamellar width.

4. Discussion

This work reports on the high-fidelity automated segmentation of myelin and IAS of myelinated axons from a multibeam serial EM image volume of human superficial white matter (i.e., $200 \times 200 \times 112 \mu\text{m}^3$) at ultra-high resolution (i.e., $32 \times 32 \times 33 \text{nm}^3$) using CNNs and deep learning. We have presented summary statistics on the inner and outer axon diameters and g-ratio of myelinated axons in this large volume of human superficial white matter tissue obtained from the temporal lobe. The automated segmentation is highly accurate thanks to the creation of a high-quality training dataset with manual annotation and meticulous handling of image artifacts in the data, achieving Dice coefficients between the segmentation results and manual segmentation of greater than 0.95. The segmented myelinated axons longer than 10 μm have inner diameters around 0.5 μm on average, outer diameters of

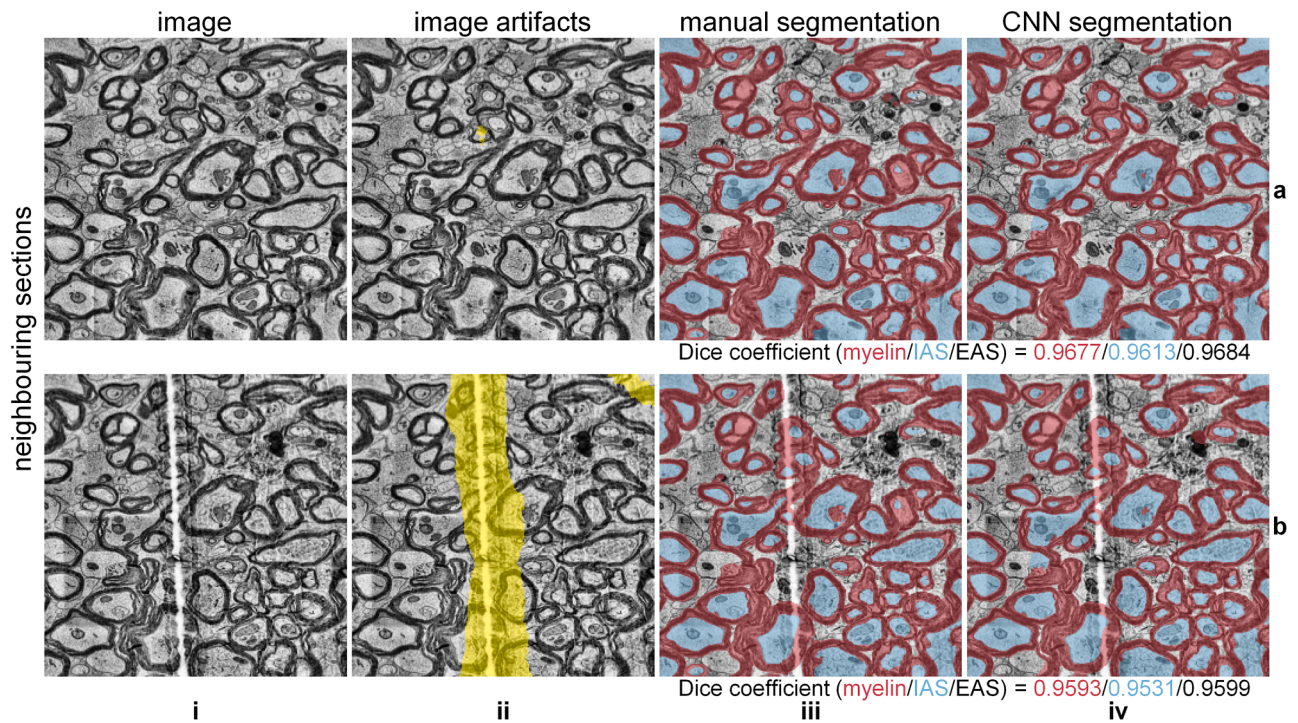


Fig. 4. Segmentation results. Two representative neighboring images are shown (a, i, and b, i) with automatically detected image artifacts (ii, yellow region) and manual (iii) and CNN (iv) segmentation results. The Dice coefficients between the manual and CNN segmentation results for myelin, intra-axonal space (IAS) and extra-axonal space (EAS) of the two image slices are listed.

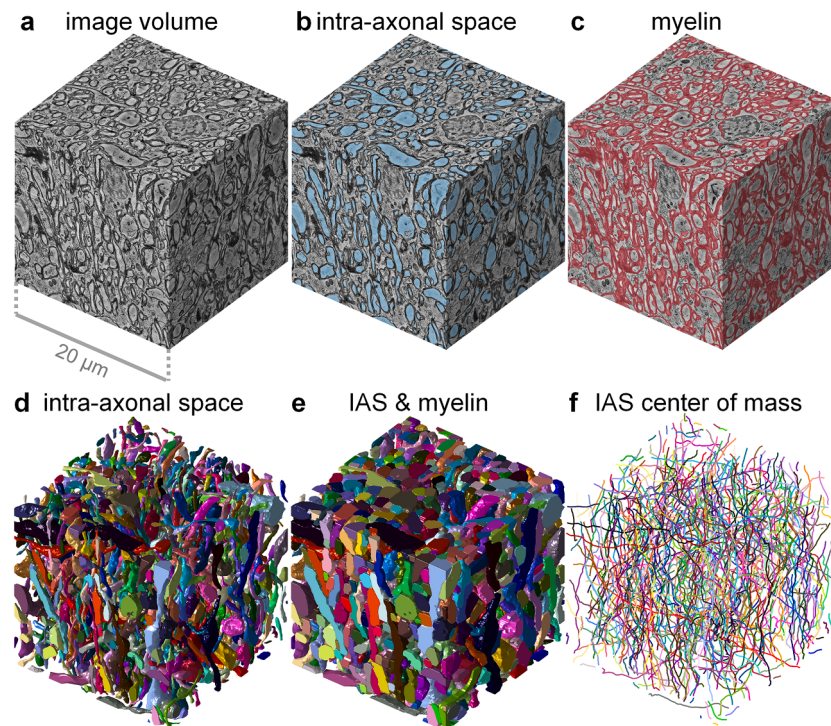


Fig. 5. Volumetric visualization. CNN segmentation of intra-axonal space (IAS) (b, d), myelin (c) and IAS plus myelin (e), and the center of mass of each IAS segment (f) of an exemplary image volume (a) of $20 \times 20 \times 20 \mu\text{m}^3$ size are shown in 3D.

approximately $1 \mu\text{m}$, and g-ratios around 0.5, with marked along-axon variations in diameter and direction.

We employed several strategies to address the lack of annotated training data, the major challenge for supervised deep learning-based segmentation. For the creation of the training dataset with manual

segmentation, we pre-trained U-Nets on a relatively large mouse EM dataset with reference myelin and IAS segmentation of myelinated axons (Lee et al., 2019) and then fine-tuned their parameters using a small amount of annotated human EM data, which was prone to over-fitting. The incorporation of transfer learning substantially improved the

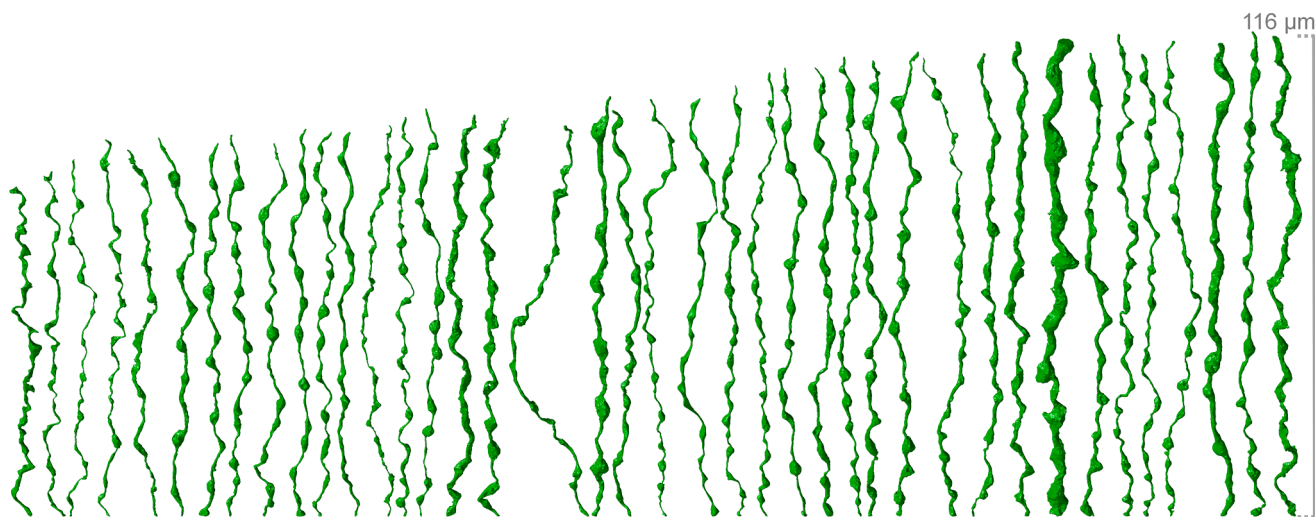


Fig. 6. Exemplary intra-axonal space segments. Volumetric rendering of forty randomly selected exemplary intra-axonal space segments of myelinated axons with lengths larger than 100 μm .

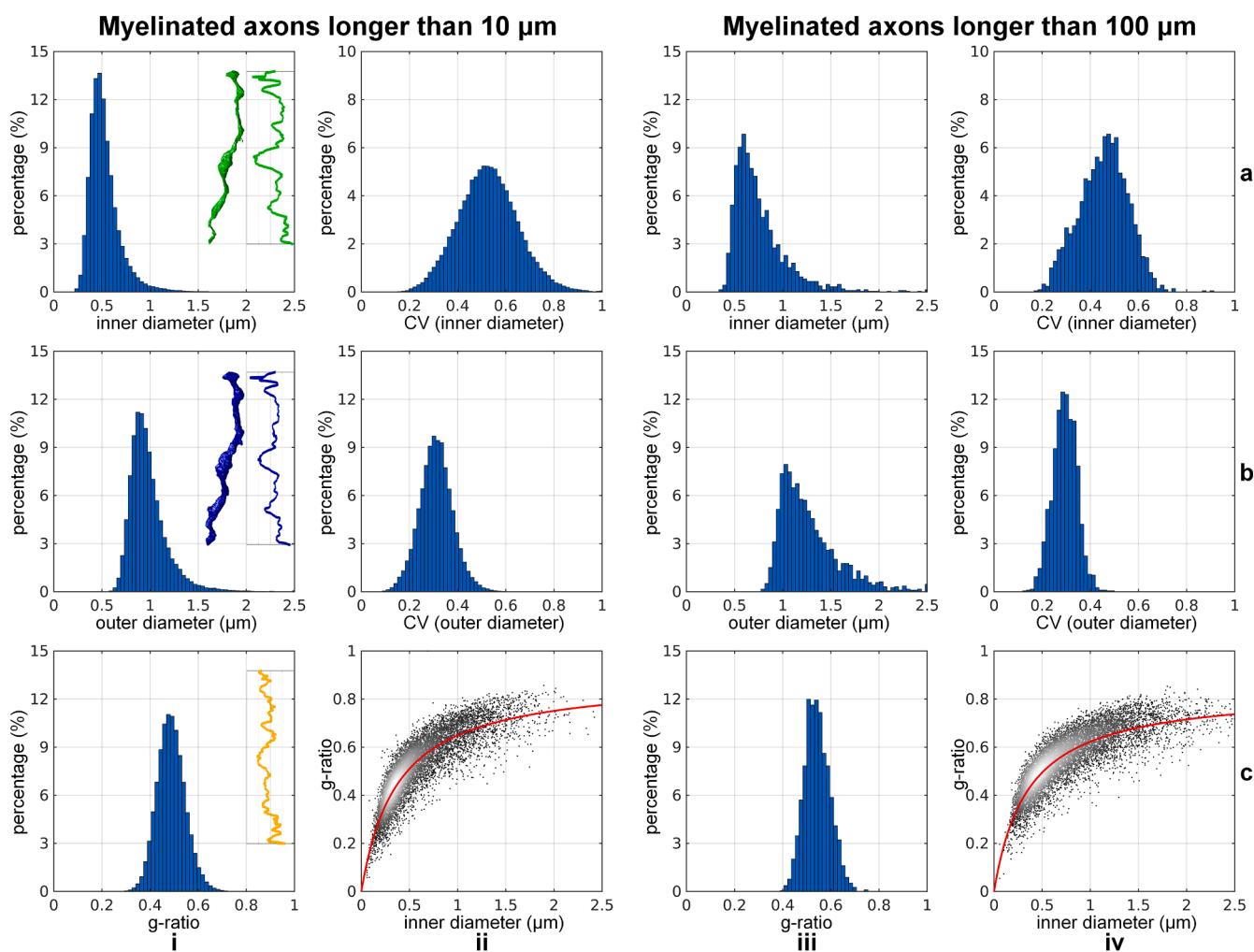


Fig. 7. Axonal characteristics. Histograms of inner axonal diameter (a, i and a, iii) and its along-axon coefficient of variation (CV) (a, ii and a, iv), outer axonal diameter (b, i and b, iii) and its along-axon CV (b, ii and b, iv), and g-ratio (c, i and c, iii) of myelinated axons longer than 10 μm and 100 μm are shown. The relationship between g-ratio and inner diameter is shown as scatter plots (c, ii and c, iv).

performance of these U-Nets and accelerated the manual clean-up process. Moreover, since the EM images in the created training dataset did not include different kinds of image artifacts in the data, the segmentation U-Net was not equipped to tackle them. We detected and zeroed out image artifacts in the data, which were not considered material to the segmentation, and augmented the training data by multiplying the EM images with inverse artifact masks. In this way, the trained U-Net learned to synthesize the segmentation results in the zeroed out regions. Finally, we adopted dropout layers in the U-Net to avoid overfitting. Dropout regularization works by randomly switching off neurons in a neural network during training, which are effectively inactive during inference. In our work, we also activated dropout layers during the inference, predicted segmentation results for an input image volume and its flipped and rotated variants, and averaged several predictions for reduced uncertainty and higher accuracy, a technique known as Monte Carlo dropout (Gal and Ghahramani, 2016). These methods work for similar studies using data acquired by EM, x-ray tomography, and other modalities.

Our work is the first study of human myelinated axons in superficial white matter using 3D EM and complements existing studies focusing on characterizing murine axons (Lee et al., 2019; Zaimi et al., 2018), non-human primate axons (Andersson et al., 2020), and human axons in deep white matter (Aboitiz et al., 1992b; Liewald et al., 2014b). The distribution of inner diameters of myelinated axons was consistent with measurements from prior EM studies in smaller samples of human corpus callosum (Aboitiz et al., 1992b) and samples in postmortem human brain (Liewald et al., 2014b). The myelinated axons in the human superficial white matter are relatively smaller than those of deep white matter, with a mean inner axon diameter of $0.53 \pm 0.17 \mu\text{m}$ for axons longer than $10 \mu\text{m}$ and $0.76 \pm 0.28 \mu\text{m}$ for axons longer than $100 \mu\text{m}$ compared to $0.63\text{--}1.34 \mu\text{m}$ in the superior longitudinal fasciculus and $0.64\text{--}0.74 \mu\text{m}$ in the corpus callosum (Liewald et al., 2014b). The myelinated axons in our sample were also smaller than those observed in mice, with an average diameter of $0.99 \pm 0.42 \mu\text{m}$ in the corpus callosum (Lee et al., 2019), as well as in monkeys, with an average diameter of $2.7 \mu\text{m}$ in the corpus callosum (Andersson et al., 2020). The myelinated axons longer than $10 \mu\text{m}$ and $100 \mu\text{m}$ in the human superficial white matter have a mean g-ratio of 0.49 ± 0.058 and 0.54 ± 0.052 respectively compared to 0.57 ± 0.09 in mouse corpus callosum (Lee et al., 2019), around 0.7 in the monkey corpus callosum (Stikov et al., 2015), as well as around 0.7 in human white matter from in vivo MRI measurement (Stikov et al., 2015; Berman et al., 2018). For reference, the theoretical optimal g-ratio for signal conduction ranges from 0.6 to 0.8 (Rushton, 1951; Chomiak and Hu, 2009; Pajevic and Basser, 2013). It is worthwhile to note that direct comparison of different studies may be confounded by variability in the sampled location, tissue fixation process and time elapsed (Tapia et al., 2012; Korogod et al., 2015; Mikula et al., 2012). Marked variation in myelinated axon diameter was observed in our results, in keeping with previous observations in mice (Lee et al., 2019; Abdollahzadeh et al., 2019), which may be resulting from different tissue preparation methods for the mouse and human samples (i.e., perfusion fixed vs. drop/immersion-fixed). The coefficients of variations of inner axon diameter of our human results were much higher than those observed in the mouse corpus callosum (Lee et al., 2019), i.e., 0.53 ± 0.12 vs. 0.28 ± 0.11 . In addition, greater variability was observed in the structure of the myelin sheath in the human superficial white matter compared to the mouse corpus callosum (Lee et al., 2019), suggesting greater biological complexity in the organization of the human myelin sheath (Ishii et al., 2009; Saliiani et al., 2017).

In addition to investigating the characteristics of myelinated axons in the human superficial white matter, the data and results presented in our work promise to inform many other studies. First, our results may serve as a starting point for training and validating much more sophisticated CNNs such as generative adversarial networks (Goodfellow et al., 2014; Souly et al., 2017), which require a larger amount of training data, for

segmenting myelin, myelinated axons and image artifacts from axon datasets acquired by EM and other imaging modalities at different spatial resolutions with improved segmentation accuracy (Tian et al., 2021). The automated segmentation results from our work could be further cleaned-up manually, with our current work contributing to a substantial reduction in the labor and time required for such manual delineation as compared to performing such a daunting task without our initial segmentation.

Second, our segmentation results provide a realistic 3D substrate of human myelinated axons for Monte Carlo simulations of water diffusion, which has relevance for the validation of in vivo microstructural imaging using diffusion MRI, an invaluable noninvasive imaging tool for neuroscientific and clinical research (Assaf et al., 2008; Veraart et al., 2020; Lee et al., 2024; Fan et al., 2019; Huang et al., 2019; Huang et al., 2020; Alexander et al., 2010; Nilsson et al., 2017). Current approaches to inferring the relationship between the diffusion MRI signal and underlying axonal structure include the use of simplistic substrates such as parallel cylinders for Monte Carlo diffusion simulations (Nilsson et al., 2017; Fan et al., 2020; Harkins et al., 2021; Burcaw et al., 2015) or at best 3D substrates segmented from white matter samples of other species (i.e., mice and non-human primates (Lee et al., 2019; Lee et al., 2020a,b; Nguyen et al., 2018; Andersson et al., 2022; Andersson et al., 2020)). Another advantage of our results is the high spatial resolution ($32 \times 32 \times 33 \text{ nm}^3$) and large sample size ($200 \times 200 \times 112 \mu\text{m}^3$), which approaches the voxel size attainable with high-resolution ex vivo diffusion MRI, in a tissue volume encompassing a total of $\sim 130\text{k}$ myelinated axons, with $>70,000$ and >2100 of them longer than 10 and $100 \mu\text{m}$, respectively. Diffusion simulations in realistic axonal geometries derived from such high resolution EM data sampled over long axonal lengths promise to aid in validating biophysical modeling of the diffusion MRI signal (e.g., axon diameter mapping) and demonstrating the effect of mesoscopic features (e.g., caliber variation and undulation along each axon) on model-fitting results, using the axonal substrates segmented from EM as a guide for the degree of geometric variation along individual axons and its effect on the diffusion signal. In comparison, current studies performed diffusion simulation using ~ 320 myelinated axons from an EM image volume of $36 \times 48 \times 20 \mu\text{m}^3$ size at $24 \times 24 \times 100 \text{ nm}^3$ resolution of the genu in corpus callosum of a mouse (Lee et al., 2019), a single astrocyte from a confocal microscopy image volume of $40 \times 40 \times 55 \mu\text{m}^3$ size at $74 \times 74 \times 299 \text{ nm}^3$ resolution of a mouse (Nguyen et al., 2018), 54 axons from an X-ray nano-holotomography volume of $140 \times 150 \times 150 \mu\text{m}^3$ size at $75 \times 75 \times 75 \text{ nm}^3$ resolution of the splenium in corpus callosum of a vervet monkey (Andersson et al., 2022; Andersson et al., 2020).

There are several limitations of our work. First, the segmented axons from our work are located in the superficial white matter, which may exhibit different characteristics (e.g., thinner myelin sheaths and smaller diameters) compared to those from major fiber tracts located in the deep white matter (Schüz and Braitenberg, 2002; Markov et al., 2013; Braitenberg and Schüz, 2013; Guevara et al., 2020). Second, the undulations and axonal beading in the fixed tissue scanned with EM could be stronger than in vivo, probably due to the long fixation time for a large sample, shrinkage during tissue preparation, and imperfect mechanical sectioning. Third, our results did not segment unmyelinated axons separately, imposing another limitation for diffusion simulations. Future work will develop more sophisticated CNNs and detailed training labels for simultaneously segmenting both myelinated and unmyelinated axons, further improving diffusion simulation and axonal quantification accuracy. Fourth, the neural network was trained to identify the pockets within the myelin sheath, which have been observed in normal aging (Xie et al., 2014). Since only one tissue sample in a human subject was available, this study was unable to distinguish the pocket caused by normal aging, pathology, or even tissue preparation. Fifth, since EM data were not collected from the deep white matter of the same subject, quantitative features of superficial white matter derived in this study were only compared to those of deep white matter from previous

literature. It is challenging to conclude whether the observed differences were biological or due to varied tissue samples and/or imaging processes. Finally, since there is no basal lamina around the axonal segment at node of Ranvier in the central nervous system (Poliak and Peles, 2003), it is difficult to distinguish nodes of Ranvier from unmyelinated axonal segments. Because the neural network only aims to segment myelinated axons and fix the interruption in the axon segmentation due to image artifact and potentially node of Ranvier, it is also challenging to further distinguish the segmentation interruption due to image artifact and node of Ranvier.

Summary

This study provides comprehensive segmentation of a large multi-beam serial EM image volume of $200 \times 200 \times 112 \mu\text{m}^3$ size for characterizing the morphometry of myelinated axons in the human superficial white matter. The segmentation of the myelin and myelinated axons was fully automated using CNNs that were trained and validated on an annotated training dataset with manual segmentation. The quantification of axonal morphometry was also automated using the RaW software. The segmentation is highly accurate, achieving Dice coefficients greater than 0.95 compared to manual segmentation and delineating 128,285 myelinated axons (70,321 longer than $10 \mu\text{m}$, 2102 longer than $100 \mu\text{m}$). Segmented myelinated axons demonstrated marked along-axon local variations in diameter and local direction, and those longer than $10 \mu\text{m}$ had inner diameters around $0.5 \mu\text{m}$, outer diameters around $1 \mu\text{m}$, and g-ratios around 0.5. This work advances our knowledge of axonal morphometry of human superficial white matter and provides a large 3D human EM dataset and segmentation results with human-level accuracy should prove useful for a variety of future studies.

CRedit authorship contribution statement

Qiyuan Tian: Writing – review & editing, Writing – original draft, Visualization, Software, Methodology, Formal analysis, Data curation, Conceptualization. **Chanon Ngamsombat:** Formal analysis, Data curation, Conceptualization. **Hong-Hsi Lee:** Writing – review & editing, Writing – original draft, Software, Formal analysis, Data curation, Conceptualization. **Daniel R. Berger:** Software, Formal analysis, Data curation, Conceptualization. **Yuelong Wu:** Data curation. **Qiuyun Fan:** Methodology, Data curation, Conceptualization. **Berkin Bilgic:** Methodology, Conceptualization. **Ziyu Li:** Software, Methodology, Formal analysis, Data curation. **Dmitry S. Novikov:** Conceptualization. **Els Fieremans:** Conceptualization. **Bruce R. Rosen:** Supervision, Resources, Funding acquisition, Conceptualization. **Jeff W. Lichtman:** Supervision, Resources, Conceptualization. **Susie Y. Huang:** Writing – review & editing, Writing – original draft, Supervision, Resources, Methodology, Funding acquisition, Conceptualization.

Declaration of competing interest

The authors declare that they have no known competing financial interests or personal relationships that could have appeared to influence the work reported in this paper.

Acknowledgments

This work was supported by the National Institutes of Health (grant numbers P41-EB015896, P41-EB030006, P41-EB017183, U24-NS135561, U24-NS137077, U01-EB026996, UM1-NS132358, R01-NS088040, R01-NS118187, R21-AG085795, R21-AG082377, S10-RR023401, S10-RR019307, S10-RR023043, K99-AG073506, DP5-OD031854).

Supplementary materials

Supplementary material associated with this article can be found, in the online version, at doi:10.1016/j.neuroimage.2025.121212.

Data availability

The EM data and the segmentation results are publicly available (<https://h01-release.storage.googleapis.com/data.html>).

References

- Abdollahzadeh, A., Belevich, I., Jokitalo, E., Sierra, A., Tohka, J., 2021. DeepACSON automated segmentation of white matter in 3D electron microscopy. *Commun. Biol.* 4, 1–14.
- Abdollahzadeh, A., Belevich, I., Jokitalo, E., Tohka, J., Sierra, A., 2019. Automated 3D Axonal Morphometry of White Matter. *Sci. Rep.* 9, 6084.
- Aboitiz, F., Scheibel, A.B., Fisher, R.S., Zaidel, E., 1992b. Individual differences in brain asymmetries and fiber composition in the human corpus callosum. *Brain Res.* 598, 154–161.
- Aboitiz, F., Scheibel, A.B., Fisher, R.S., Zaidel, E., 1992a. Fiber composition of the human corpus callosum. *Brain Res.* 598, 143–153.
- Alexander, D.C., et al., 2010. Orientationally invariant indices of axon diameter and density from diffusion MRI. *NeuroImage* 52, 1374–1389.
- Andersson, M., et al., 2020. Axon morphology is modulated by the local environment and impacts the noninvasive investigation of its structure–function relationship. *Proceedi. Natl. Acad. Sci.* 117, 33649–33659.
- Andersson, M., et al., 2022. Does powder averaging remove dispersion bias in diffusion MRI diameter estimates within real 3D axonal architectures? *NeuroImage* 248, 118718.
- Assaf, Y., Blumenfeld-Katzir, T., Yovel, Y., Basser, P.J., 2008. AxCaliber: a method for measuring axon diameter distribution from diffusion MRI. *Magn. Reson. Med.* 59, 1347–1354.
- Baena, V., Schalek, R.L., Lichtman, J.W., Terasaki, M., 2019. Serial-section electron microscopy using automated tape-collecting ultramicrotome (ATUM). *Method. Cell Biol.* 152, 41–67.
- Barazany, D., Basser, P.J., Assaf, Y., 2009. In vivo measurement of axon diameter distribution in the corpus callosum of rat brain. *Brain* 132, 1210–1220.
- Barkovich, A.J., 2000. Concepts of myelin and myelination in neuroradiology. *Am. J. Neuroradiol.* 21, 1099–1109.
- Berger, D.R., Seung, H.S., Lichtman, J.W., 2018. VAST (volume annotation and segmentation tool): efficient manual and semi-automatic labeling of large 3D image stacks. *Front. Neur. Circuit.* 12, 88.
- Berman, S., West, K.L., Does, M.D., Yeatman, J.D., Mezer, A.A., 2018. Evaluating g-ratio weighted changes in the corpus callosum as a function of age and sex. *NeuroImage* 182, 304–313.
- Berning, M., Boergens, K.M., Helmstaedter, M., 2015. SegEM: efficient image analysis for high-resolution connectomics. *Neuron* 87, 1193–1206.
- Berthold, C.-H., Nilsson, I., Rydmark, M., 1983. Axon diameter and myelin sheath thickness in nerve fibres of the ventral spinal root of the seventh lumbar nerve of the adult and developing cat. *J. Anat.* 136, 483.
- Braitenberg, V., Schüz, A., 2013. *Cortex: Statistics and Geometry of Neuronal Connectivity*. Springer Science & Business Media.
- Burcaw, L.M., Fieremans, E., Novikov, D.S., 2015. Mesoscopic structure of neuronal tracts from time-dependent diffusion. *NeuroImage* 114, 18–37.
- Butt, A.M., Berry, M., 2000. Oligodendrocytes and the control of myelination in vivo: new insights from the rat anterior medullary velum. *J. Neurosci. Res.* 59, 477–488.
- Chomiak, T., Hu, B., 2009. What is the optimal value of the g-ratio for myelinated fibers in the rat CNS? A theoretical approach. *PLoS One* 4, e7754.
- Dorkenwald, S., et al., 2017. Automated synaptic connectivity inference for volume electron microscopy. *Nat. Method.* 14, 435–442.
- Eberle, A.L., Zeidler, D., 2018. Multi-beam scanning electron microscopy for high-throughput imaging in connectomics research. *Front. Neuroanat.* 12, 112.
- Falk, T., et al., 2019. U-Net: deep learning for cell counting, detection, and morphometry. *Nat. Method.* 16, 67–70.
- Fan, Q., et al., 2019. Age-related alterations in axonal microstructure in the corpus callosum measured by high-gradient diffusion MRI. *NeuroImage* 191, 325–336.
- Fan, Q., et al., 2020. Axon diameter index estimation independent of fiber orientation distribution using high-gradient diffusion MRI. *NeuroImage*, 117197.
- Gal, Y., Ghahramani, Z., 2016. Dropout as a bayesian approximation: Representing model uncertainty in deep learning. In: *international conference on machine learning*. PMLR, pp. 1050–1059.
- Goodfellow, I., et al., 2014. Generative adversarial nets. *Adv. Neur. Inf. Process. Syst.* 27, 2672–2680.
- Guevara, M., Guevara, P., Román, C., Mangin, J.-F., 2020. Superficial white matter: a review on the dMRI analysis methods and applications. *NeuroImage*, 116673.
- Harkins, K.D., Beaulieu, C., Xu, J., Gore, J.C., Does, M.D., 2021. A simple estimate of axon size with diffusion MRI. *NeuroImage* 227, 117619.
- Huang, S.Y., et al., 2019. Corpus callosum axon diameter relates to cognitive impairment in multiple sclerosis. *Ann. Clin. Transl. Neurol.* 6, 882–892.

- Huang, S.Y., et al., 2020. High-gradient diffusion MRI reveals distinct estimates of axon diameter index within different white matter tracts in the in vivo human brain. *Brain Struct. Funct.* 225, 1277–1291.
- Ishii, A., et al., 2009. Human myelin proteome and comparative analysis with mouse myelin. In: *Proceedings of the National Academy of Sciences of the United States of America*, 106, pp. 14605–14610.
- Januszewski, M., et al., 2018. High-precision automated reconstruction of neurons with flood-filling networks. *Nat. Method.* 15, 605–610.
- Jurrus, E., et al., 2009. Axon tracking in serial block-face scanning electron microscopy. *Med. Image Anal.* 13, 180–188.
- Kaynig, V., et al., 2015. Large-scale automatic reconstruction of neuronal processes from electron microscopy images. *Med. Image Anal.* 22, 77–88.
- Kleinnijenhuis, M., et al., A 3D electron microscopy segmentation pipeline for hyper-realistic diffusion simulations. In *Proceedings of the 25th Annual Meeting of the International Society for Magnetic Resonance in Medicine (ISMRM), Honolulu, Hawaii, USA, 2017*: p. 1090.
- Korogod, N., Petersen, C.C., Knott, G.W., 2015. Ultrastructural analysis of adult mouse neocortex comparing aldehyde perfusion with cryo fixation. *Elife* 4, e05793.
- Lee, H.-H., et al., 2019. Along-axon diameter variation and axonal orientation dispersion revealed with 3D electron microscopy: implications for quantifying brain white matter microstructure with histology and diffusion MRI. *Brain Struct. Funct.* 224, 1469–1488.
- Lee, H.H., et al., 2024. The effects of axonal beading and undulation on axonal diameter estimation from diffusion MRI: insights from simulations in human axons segmented from three-dimensional electron microscopy. *NMR Biomed.* e5087.
- Lee, H.-H., Jespersen, S.N., Fieremans, E., Novikov, D.S., 2020b. The impact of realistic axonal shape on axon diameter estimation using diffusion MRI. *NeuroImage* 223, 117228.
- Lee, H.-H., Papaioannou, A., Kim, S.-L., Novikov, D.S., Fieremans, E., 2020a. A time-dependent diffusion MRI signature of axon caliber variations and beading. *Commun. Biol.* 3, 1–13.
- Liewald, D., Miller, R., Logothetis, N., Wagner, H.J., Schuz, A., 2014b. Distribution of axon diameters in cortical white matter: an electron-microscopic study on three human brains and a macaque. *Biol. Cybern.* 108, 541–557.
- Liewald, D., Miller, R., Logothetis, N., Wagner, H.-J., Schüz, A., 2014a. Distribution of axon diameters in cortical white matter: an electron-microscopic study on three human brains and a macaque. *Biol. Cybern.* 108, 541–557.
- Little, G.J., Heath, J.W., 1994. Morphometric analysis of axons myelinated during adult life in the mouse superior cervical ganglion. *J. Anat.* 184, 387.
- Markov, N.T., et al., 2013. Cortical high-density counterstream architectures. *Science* 342.
- Mikula, S., Binding, J., Denk, W., 2012. Staining and embedding the whole mouse brain for electron microscopy. *Nat. Method.* 9, 1198–1201.
- Motta, A., et al., 2019. Dense connectomic reconstruction in layer 4 of the somatosensory cortex. *Science* 366.
- Nazeri, A., et al., 2013. Alterations of superficial white matter in schizophrenia and relationship to cognitive performance. *Neuropsychopharmacology* 38, 1954–1962.
- Nguyen, K.-V., Hernández-Garzón, E., Valette, J., 2018. Efficient GPU-based Monte-Carlo simulation of diffusion in real astrocytes reconstructed from confocal microscopy. *J. Magnet. Reson.* 296, 188–199.
- Nilsson, M., Lasič, S., Drobniak, I., Topgaard, D., Westin, C.F., 2017. Resolution limit of cylinder diameter estimation by diffusion MRI: the impact of gradient waveform and orientation dispersion. *NMR Biomed.* 30, e3711.
- Pajević, S., Basser, P.J., 2013. An optimum principle predicts the distribution of axon diameters in normal white matter. *PLoS One* 8, e54095.
- Parazzini, C., Baldoli, C., Scotti, G., Triulzi, F., 2002. Terminal zones of myelination: MR evaluation of children aged 20–40 months. *Am. J. Neuroradiol.* 23, 1669–1673.
- Perge, J.A., Koch, K., Miller, R., Sterling, P., Balasubramanian, V., 2009. How the optic nerve allocates space, energy capacity, and information. *J. Neurosci.* 29, 7917–7928.
- Phillips, O.R., et al., 2011. Mapping corticocortical structural integrity in schizophrenia and effects of genetic liability. *Biol. Psychiatry* 70, 680–689.
- Phillips, O.R., et al., 2016. The superficial white matter in Alzheimer's disease. *Hum. Brain Mapp.* 37, 1321–1334.
- Poliak, S., Peles, E., 2003. The local differentiation of myelinated axons at nodes of Ranvier. *Nat. Rev. Neurosci.* 4, 968–980.
- Ronneberger, O., Fischer, P., Brox, T., 2015. U-net: Convolutional networks for biomedical image segmentation. In: *Medical image computing and computer-assisted intervention-MICCAI 2015: 18th international conference, Munich, Germany, October 5-9, 2015, proceedings, part III 18*. Springer international publishing, pp. 234–241.
- Rushton, W., 1951. A theory of the effects of fibre size in medullated nerve. *J. Physiol. (Lond.)* 115, 101.
- Saliani, A., et al., 2017. Axon and Myelin Morphology in Animal and Human Spinal Cord. *Front. Neuroanat.* 11, 129.
- Schüz, A., Braitenberg, V., 2002. The human cortical white matter: quantitative aspects of cortico-cortical long-range connectivity. *Cort. Ar.: Unit. Divers.* 377–385.
- Sepelband, F., Alexander, D.C., Kurniawan, N.D., Reutens, D.C., Yang, Z., 2016. Towards higher sensitivity and stability of axon diameter estimation with diffusion-weighted MRI. *NMR Biomed.* 29, 293–308.
- Shapson-Coe, A., et al., 2024. A petavoxel fragment of human cerebral cortex reconstructed at nanoscale resolution. *Science* 384, eadk4858.
- Shukla, D.K., Keehn, B., Smylie, D.M., Müller, R.-A., 2011. Microstructural abnormalities of short-distance white matter tracts in autism spectrum disorder. *Neuropsychologia* 49, 1378–1382.
- Sommer, C., Straehle, C., Koethe, U., Hamprecht, F.A., 2011. In: *IEEE international symposium on biomedical imaging: From nano to macro*. IEEE, pp. 230–233.
- Souly, N., Spampinato, C., & Shah, M., "Semi supervised semantic segmentation using generative adversarial network." In *Proceedings of the IEEE international conference on computer vision*, pp. 5688-5696. 2017.
- Stikov, N., et al., 2015. In vivo histology of the myelin g-ratio with magnetic resonance imaging. *NeuroImage* 118, 397–405.
- Sundaram, S.K., et al., 2008. Diffusion tensor imaging of frontal lobe in autism spectrum disorder. *Cerebr. Cort.* 18, 2659–2665.
- Tapia, J.C., et al., 2012. High-contrast en bloc staining of neuronal tissue for field emission scanning electron microscopy. *Nat. Protoc.* 7, 193–206.
- Tian, Q., Bilgic, B., Fan, Q., Ngamsombat, G.C., Zertsakaya, N., Fultz, N.E., Ohringer, N.A., Chaudhari, A.S., Hu, Y., Witzel, T., Setsompop, K., Polimeni, J.R., Huang, S.Y., 2021. Improving in vivo human cerebral cortical surface reconstruction using data-driven super-resolution. *Cerebr. Cortex.* 31, 463–482.
- Van der Knaap, M.S., Valk, J., 2005. *Magnetic Resonance of Myelination and Myelin Disorders*. Springer Science & Business Media.
- Veraart, J., et al., 2020. Noninvasive quantification of axon radii using diffusion MRI. *Elife* 9, e49855.
- West, K.L., Kelm, N.D., Carson, R.P., Does, M.D., 2015. Quantitative analysis of mouse corpus callosum from electron microscopy images. *Data Brief* 5, 124–128.
- Wu, M., Kumar, A., Yang, S., 2016. Development and aging of superficial white matter myelin from young adulthood to old age: mapping by vertex-based surface statistics (VBSS). *Hum. Brain Mapp.* 37, 1759–1769.
- Xie, F., Liang, P., Fu, H., Zhang, J.C., Chen, J., 2014. Effects of normal aging on myelin sheath ultrastructures in the somatic sensorimotor system of rats. *Mol. Med. Rep.* 10, 459–466.
- Zaimi, A., et al., 2018. AxonDeepSeg: automatic axon and myelin segmentation from microscopy data using convolutional neural networks. *Sci. Rep.* 8, 3816.